Incomplete Partition Type-II Cochlear Malformations: Delineating the 3D Structure from Digitised Human Histopathological Specimens

Short running head: IP-II 3D histopathology

Chloe Swords MA MRCS[1,2,3], Alexander Geerardyn MD[2,3,4], Mengyu Zhu MS[2,3], Jennifer T. O'Malley[2,3,5], Peizhe Wu MD[3,5], Julie G. Arenberg PhD CCC-A[3,5,6], Archana Podury[2,3], Cecilia Brassett FRCS[1], Manohar Bance MB FRCS[7], Alicia M. Quesnel MD[2,3]

1. Department of Physiology, Development and Neuroscience, University of Cambridge, Cambridge, UK. 2. Otopathology Laboratory, Massachusetts Eye and Ear, Boston, MA, USA. 3. Department of Otolaryngology – Head and Neck Surgery, Harvard Medical School, Boston, MA, USA. 4. ExpORL, Department of Neurosciences, Katholieke Universiteit Leuven, Leuven, Belgium. 5. Eaton-Peabody Laboratories, Massachusetts Eye and Ear, Boston, MA, USA. 6. Audiology Division, Massachusetts Eye and Ear, Boston, MA, USA. 7. Department of Clinical Neurosciences, University of Cambridge, Cambridge, UK

Corresponding author:

Alicia Quesnel, MD, Otopathology Laboratory, Department of Otolaryngology, Massachusetts Eye and Ear Infirmary, 243 Charles Street, Boston, MA, 02114

Phone: (617) 573-3503, Fax: (617) 573-3939

Email: Alicia_Quesnel@meei.harvard.edu

Source of Funding: Royal College of Surgeons (England) (CS), Anatomical Society (CS), Baroness de Turckheim fund (CS), Wellcome Trust Developing Concept Fund (RG93172/BANCE/40181, MLB), the Biomedical Research Centre Cambridge (MLB), NIH/NIDCD U24DC013983 (AMQ, MZ) and U24DC020849 (AMQ), Research Foundation Flanders (1SD3322N;V414121N, AG).

Conflicts of Interest: AMQ: Frequency Therapeutics (consulting, sponsored research agreement), Grace Medical (sponsored research, licensed patent), Alcon (consulting). MLB: Decibel Therapeutics (consulting), Advanced Bionics (grant), Cochlear (grant), MEDEL (grant), Oticon Medical (grant). JGA: Frequency Therapeutics (consulting).

Keywords: Cochlear implant, inner ear malformation, cochlear malformation, histopathology, incomplete partition

Abstract

Hypothesis

There are clinically-relevant differences in scalae anatomy and spiral ganglion neuron (SGN) quantity between incomplete partition type II (IP-II) and normal cochleae.

Background

IP-II is a commonly implanted cochlear malformation. Detailed knowledge of intracochlear three-dimensional (3D) morphology may assist with cochlear implant (CI) electrode selection/design and enable optimization of audiologic programming based on SGN maps.

Methods

IP-II (n=11) human temporal bone histological specimens were identified from the NIDCD National Temporal Bone Registry and digitised. The cochlear duct, scalae, and surgically-relevant anatomy were reconstructed in 3D. A machine learning algorithm was applied to map the location and number of SGNs.

Results

3D scalae morphology of the basal turn was normal. Scala tympani (ST) remained isolated for 540° before fusing with scala vestibuli (SV). Mean ST volume reduced below $1mm^2$ after the first 340°. Scala media was a distinct endolymphatic compartment throughout; mean cochlear duct length was 28mm+/-3mm SD. SGNs were reduced compared to age-matched norms (mean 48%, range 5-90%). In some cases, SGNs failed to ascend Rosenthal's canal, remaining in an abnormal basalward modiolar location. Two forms of IP-II were seen: type A and type B. The majority (98-100%) of SGN were located in the basal modiolus in type B IP-II, compared to 76-85% in type A.

Conclusion

Hallmark features of IP-II cochleae include: (1) fusion of the ST and SV at a mean of 540°, (2) highly variable and overall reduced SGN quantity compared to normative controls (3) abnormal SGN distribution with cell bodies failing to ascend Rosenthal's canal.

Introduction

Cochlear implants (CI) are surgically-implanted neuroprostheses for the management of severe-to-profound hearing loss in patients with or without inner ear malformations (IEM). They enable hearing sensation by 'electrically' stimulating spiral ganglion neurons (SGNs), bypassing acoustic hearing. Over 800,000 individuals with hearing impairment have received CIs worldwide(1), and *c.*20% of children with sensorineural hearing loss have a radiologically discernible IEM(2–4). Since their introduction, technological advances have improved CI performance(5). This was achieved by advanced anatomical knowledge of how implants interface with the normal cochlea and auditory nerve, using both histology and high-resolution imaging(6). For instance, SGNs are known to be tonotopically arranged within Rosenthal's canal(7,8). This has enabled derivation of an average frequency-position in normal cochleae(9). In contrast, a similar understanding about IEMs is lacking.

In the past two decades, Sennaroğlu *et al.* have redefined the classification of IEMs(10–12). The scheme defined IEMs as labyrinthine aplasia, cochlear aplasia, common cavity, cochlear hypoplasia types I–IV and incomplete partition types I–III (IP-I to III). CI performance is variable, but IP-II patients appeared to perform best among patients with IEMs when comparing post-operative speech perception(13). Sennaroğlu's classifications were based on matched radiographic and surgical cases, with subsequent examination of histopathology slides(14). Dhanasingh *et al.* reconstructed computed tomography (CT) in three-dimensions (3D) to further inform our understanding of IEM anatomy(15). However, clinical CT is limited by its low-resolution (*c.*400-microns(µm)) and greyscale features, precluding an understanding of scalae compartments, soft tissue, and neural elements. Digitised otopathology sections of the inner ear enable visualization of high-resolution histological structures in 3D and mapping of architectural features both within and surrounding an anatomical structure.

Our objectives were, firstly, to delineate the 3D morphology of IP-II malformations, and secondly, to describe and quantify SGN populations and their variability. We speculate on the implications for cochlear implantation.

Materials and Methods

Temporal bone harvesting and preparation

Temporal bone specimens were derived from the Massachusetts Eye and Ear Otopathology Laboratory collection. The methods were approved by the Mass General Brigham Institutional Review Board (Protocol number 2019P003755). Prior to death, informed consent was obtained from donors for inclusion in the National Institute on Deafness and Other Communication Disorders (NIDCD) National Temporal Bone, Hearing and Balance Pathology Resource Registry. This contains pertinent past medical history and a histopathological report written by an otopathological expert.

Temporal bone specimens underwent routine histologic processing with fixation, decalcification, dehydration, and embedment in celloidin. The preservation techniques have evolved over many years; specimens were fixed with Heidenhain's Susa or 10% formalin, and decalcified with trichloroacetic acid or ethylenediaminetetraacetic acid for between 35-316 days. Specimens were sectioned at a thickness of 20µm. Every 10th section was stained with haematoxylin and eosin (H&E) and mounted on a glass slide. The stained sections were digitised using Aperio AT2 Digital Scanner (Leica Biosystems, Vista, CA, USA).

Case selection

The NIDCD database was searched using pre-defined search terms to identify IEM candidates (**Supplementary Material 1**). Prior to this study, the database did not include the updated Sennaroğlu IEM classification(10–12,16,17). Two authors independently verified the classification of each specimen (CS/AMQ). Following classification, IP-II cochleae were selected for analysis (Normal cochlea for comparison **Figure 1A**; IP-II **Figure 1B**).

Clinical data

Demographics, past medical history, and available audiometric data were reviewed.

2D histologic assessment

The location of scala communis (SC) and the three interscalar ridges (IS1 to 3), as defined by Makary(18), were identified on horizontal sections. IS1 is the most proximal ridge, separating the lower basal from the lower middle turn; IS2 separates the upper basal from the upper middle turn; and IS3 separates the lower middle from the apical turn. In addition, facial nerve and vestibular system morphology, such as the vestibule and semicircular canals, were described.

Preparation of slides for 3D Reconstruction

To enable compatibility with 3D segmentation software, images were cropped around the cochlea, down-sampled, aligned, and merged into a hyperstack. Hyperstacks were created to account for the nine unstained sections between every stained section(19). This enabled more detailed and representative segmentation(20). This was performed in Amira (FEI Company, Hillsboro, OR, version 2019.1) and Fiji (v2.5.0)(21). Due to the size of hyperstacks, the vestibular system could not be included.

3D reconstruction of the cochlea

Amira was used to segment images to produce digital surface reconstructions. Specifically, the morphology of the bony cochlea, scalae, Rosenthal's canal, hook region, bony niche and round window (RW) were delineated. The osseous spiral lamina, spiral ligament, basilar membrane and secondary spiral lamina were reconstructed adjacent to the RW and hook regions. When the scalae fused, they were designated as SC and reconstructed separately (**Figure 1B-C**). Surface

reconstructions were saved as .stl files. Using the B-spline function, landmark coordinates were generated for the centre of the cochlear duct and Rosenthal's canal. Rosenthal's canal and cochlear duct length (CDL) were measured using the 'arclength' function (MATLAB R2021a, MathWorks Inc., Massachusetts, USA).

3D measurements

To enable comparison, images of the right ear were inverted to appear as left ears. Scala tympani (ST) reconstructions were imported into MATLAB. Using a custom-built script, the ST mesh was divided into 2D cross-sections at 100 equally-spaced slices from the RW to the start of the SC (**Figure 2A**). The cross-sectional area of each slice was calculated using the MATLAB function 'polygonArea3d'(20).

The A-value (longest diameter of the cochlea in the basal plane(22) from the centre of the RW to the far lateral wall, intersecting the central modiolar) and B-value (cochlear width perpendicular to the A-value, intersecting the central modiolus) (**Figure 1D**) were measured.

Functional RW diameter measurements were obtained using the 3D circle-measuring tool in Amira. The RW short diameter was defined by the diameter of the largest circle fitting within the bony annulus(23). Reconstructions were aligned at an approximation of the surgical plane, defined as the orientation of the cochlea relative to the facial recess prior to CI surgery.

Vestibular aqueduct measurements

The widths of the vestibular aqueduct (VA) at the midpoint and at the operculum (the latter defined from the edge of the operculum to the posterior surface of the petrous bone at 90^{o}) were measured (**Supplementary Material 2**). Enlarged vestibular aqueduct (EVA) was defined as a VA midpoint of >1.5mm(24).

Location of Spiral Ganglion Cells

SGN location was identified using an automated machine learning approach (Wu, O'Malley, Liberman. Neural degeneration in human cochleae: machine-learning counts and 3D mapping in archival sections. *Under peer review* (2023)). A map showing which cells were counted was produced by the machine learning program (**Supplementary Material 2C**). The accuracy of the algorithm depends on cell morphology (no morphologic difference in IP-II SGNs). In addition, SGNs that were not identified using the automated methodology were counted manually and combined with the original count. SGNs were counted when there was a nucleus visible, and therefore the Konigsmark correction factor (0.68) was used(25). Counts were compared to age-matched normative published data (before corrections were made)(26).

Statistical analysis

Statistical analysis was performed in MATLAB. Following consultation with a medical statistician, only one ear was included from the same patient to avoid over-representation of a single individual. Data were tested for normality using the Kolmogorov-Smirnov test. The mean and standard deviation (SD) were calculated. Unpaired t-test was performed to compare IP-II and normal cochleae, with $p<0.05$ deemed significant.

Results

Summary of cases

Of the 456 cases identified by database searching, 71 had IEMs. These were classified according to Sennaroğlu's classification (**Supplementary Material 3)**. There were 11 IP-II ears from seven patients. Descriptive assessments are summarised in **Supplementary Material 4**. Three patients (3/11 ears) had an underlying syndrome: trisomy-18, Kleefstra, and Cornelia de Lange syndrome. One patient (2/11 ears) had a history of congenital syphilis. One patient contracted *Staphylococcus aureus* meningitis 6 weeks before death (2/11 ears), resulting in explantation of his right CI. One patient contracted measles in infancy (2/11 ears). All of the eight cases with formal assessment of their hearing had sensorineural hearing loss. One patient had undergone bilateral CI, via cochleostomy.

Five cases had EVA (**Supplementary Material 4**). The majority (91%) of cases had defective IS2 (separating upper basal and upper middle turn) and IS3 angles (separating lower middle from apical turn); one had an isolated IS3 defect. The bony vestibule, as qualitatively assessed by an experienced histopathologist, was enlarged in 9/11 ears, although the semicircular canals were only malformed in 2/11 ears. The facial nerve was in a typical position in 9/11 specimens (**Supplementary Material 4**); the descending segment was more lateral in one, and in contact with the stapes suprastructure in the other.

Morphology of bony cochlea and scalae compartments

The mean cochlear volume was 0.067ml (SD-0.012). Mean A- and B-values were 8.43mm (SD-0.48) and 6.03mm (SD-0.78), respectively (**Figure 1D**). All cochleae exhibited a coiled shape with 2.5 turns, albeit with an abnormal appearance to the middle and upper turns. Regarding the bony structure,

two distinct appearances were seen depending on the morphology of the upper two turns (**Figure 2B-C**). The first group had a widened middle turn, with an apical turn of similar width (n=6). The second group had a shorter middle turn, with an apical turn of smaller width.

Intralabyrinthine components were visible in 9/11 ears (obscured in two due to post-meningitic changes). ST and SV were distinct in the first 360°, becoming fused in the middle turn. Where the fusion occurred, the resultant compartment was referred to as SC (**Figure 1C,2D**). The first compartments to fuse were the basal turn SV and middle turn ST. The basal ST remained an isolated compartment in the first 540° in all cochleae (**Figure 2E**). The ST cross-sectional area in the first turn was significantly smaller than normal cochleae (mean normal 1.44mm^2, IP-II 1.41mm^2, p=0.0004; the first 50° was excluded to prevent incorporation of spurious results from the hook region. Normal data was obtained from unpublished micro-computed tomography (microCT) results (derived from 80 specimen) using scanning and analysis techniques described previously(22)) (**Figure 2A,2F**). Despite this significant difference, the reduced values for the first turn of IP-II cochleae may not be functionally significant. After ~340°, the cross-sectional area decreased to <1mm^2 (range: 215-490°, compared to >450° in the normal cochleae), although one can observe a transient increase in area apical to 400°, related to the ascending trajectory of the cochlea. At 90°, 180°, 270° and 360° of insertion (from base to apex), the mean(±SD) cross-sectional area was 1.75(0.38), 1.42(0.41), 1.11(0.21) and 0.97(0.27)mm^2 , respectively.

Scala media (SM) was present as a separate compartment for 2.5 turns in all cases (**Figure 3A-F**). Additional SM compartments were present in 6/11 ears, present as either a small additional compartment, partial expansion into the modiolus, or complete modiolar expansion (**Figure 3B&E,C&F**). The SM was visible in 3/5 EVA cases; it was expanded in all. Complete SM modiolar expansion was not present in any cases with a normal VA.

Spiral ganglion neurons

Numbers of SGNs varied significantly, ranging from 1,292 to 20,692, or 5-90% of age-matched normative published data(27). **Table 1** shows the absolute SGN counts. Most cochleae exhibited a Rosenthal's canal that projected to the middle turn (mean length 9.99mm, SD-1.5) (**Figure 4A**), although SGNs were sparse in the middle compared to the basal turn. Peripheral axons were present throughout the cochlea in the majority of cases (8/9 ears; not visible in 2).

Two cochleae showed SGN collections at the modiolar base, which had not migrated superiorly to the apical modiolus (**Figure 4B-E,5**). Despite failing to migrate, the age-matched SGN counts were 12,396 and 20,692 (54% and 90% of age-matched normal). However, in these cases, peripheral axons were longer than expected owing to their path from SGNs at the modiolar base to the apical organ of Corti. The third cochleae (2/L, **Figure 5**) with SGN collections only at the modiolar base had very low total SGN count, with sparse peripheral processes, so may represent a different developmental process. SGNs were present within the IAC in six specimens (**Figure 4F**).

Two distinct bony cochlear morphologies were identified (see above; **Figure 5**). The average SGN counts for type A were 7,995 (age-adjusted 50%, range 32-80%) and type B were 9918 (age-adjusted 45%, range 5-90%). In type A, 76-85% of SGNs were located in the basal turn; in type B, 98-100% of SGNs were located in the basal turn. Group sizes were too small for quantitative statistical comparisons.

RW and hook region of the cochlea

All cochleae had a defined RW membrane, which was recessed within the RW niche, with a convex appearance towards the ST (**Supplementary Material 5**). At the anterolateral aspect of the RW membrane was the crista fenestra. The mean RW membrane short diameter was 1.00mm (SD-0.21, range:0.71-1.29). The position of the RW membrane was variable: more posterior in some cases and located on the inferolateral aspect of the ST. The ST, along with the osseous spiral lamina, bridge and basilar membrane, curved anteroinferiorly and laterally, exhibiting a 'hook region', as in normal cochleae. The secondary spiral lamina projected from the superior aspect of the RW membrane and arched posteriorly. It did not merge with the basilar membrane or osseous spiral lamina.

Discussion

This study comprehensively describes the 3D morphology of 11 IP-II cochleae. There was variation in gross morphology, with two principal shapes identified. Even within these subsets, differences existed in scalae morphology and the neural interface. A subsection of specimens had concurrent EVA; where visible, these EVA specimens exhibited abnormal SM, although perilymphatic compartments were similar to other IP-II cochleae. The location and numbers of SGNs varied (1,292-20,692; 5-90% of age-matched norms).

Surgical anatomy considerations

Some aspects of anatomy relevant to cochlear implantation, via the facial recess approach, were similar to normal cochleae, including the facial nerve being in a typical position in 9/11 specimens (lateral descending segment (n=1), contact with stapes suprastructure (n=1)(28)). The RW niche and hook regions had conventional appearances, suggesting that surgeons should encounter a classical niche requiring drilling, and use a standard trajectory when inserting the implant to prevent mechanical intraluminal damage. Notably, the RW membrane short diameter measured slightly smaller than published normal values (1mm *vs.* 1.3mm)(23). Our RW measurements excluded the crista fenestra; to facilitate implantation, some cases may require an extended RW approach or cochleostomy(29), being mindful that intraluminal bone dust has been associated with secondary inflammation and fibro-osseous tissue formation(30).

Some notable intracochlear differences were identified. As current imaging modalities are insufficient to identify these findings, the following conclusions are important for implant surgeons.

The overall 2D size and CDL measures were slightly smaller than published norms. A variety of CDL measurements have been published, with normative mean estimates ranging from 33-37mm (measured by 3D reconstruction) *vs.* 28mm in our series(31). The only other published IP-II CDL was

based upon microCT of a *Slc26a4*-null mouse model; this study also identified a shorter CDL compared to normal(32). Our mean IP-II cochlear volume was 0.067ml; published normal values vary from 0.065ml (n=184, measured by active shape model(33)) to 0.078ml (n=45, segmentation of clinical imaging(34)).

Our study identified that ST cross-sectional diameter was smaller than normal, and reduced <1mm^2 beyond the first turn. It should be noted that, whilst being a statistically significant difference, the mean cross-sectional area in the first 360^o may not confer a functional difference (1.44mm^2 *vs.* 1.41mm^2). The IP-II mean A- and B-values were 8.43 and 6.03mm respectively in our study, whereas a series of 30 normal cochleae evaluated on microCT found larger values of 9.0 and 6.9mm respectively(35). Our measurements in IP-II differs from published studies of IEM based upon clinical imaging(34), likely representing a margin of error when performing these measurements on lower-resolution imaging as compared to histology. Given that CIs are not inserted all the way to the apex, (average angular insertion depths: 420^o, although up to 600^o for some manufacturers)(33), the first 360^o ST-neural interface is likely to be the most important consideration for implantation.

The relationship of neural elements to the ST represents the CI electrode-neural interface. Firstly, there was a sparsity of apical SGNs compared to the basal population, particularly in IP-II type B. In two cases of type B, they were absent apically, with the intended population located in the modiolar base. However, these SGNs were still connected via peripheral processes to the apical organ of Corti. The processes were longer than normal and located in the middle turn of the ST, without a protective modiolus to support the thin lamina. Normally, peripheral processes are securely located, reducing the likelihood of implant-related trauma. Surgeons should be mindful of the potential for such features being present beyond the basal turn, to avoid mechanical trauma by over-inserting the electrode beyond the first turn, particularly in hearing preservation cases(36).

Secondly, even in IP-II cases where some of the SGNs ascended beyond the basal turn, the majority of SGNs were located in the basal turn, rather than being spaced throughout Rosenthal's canal. In addition, Rosenthal's canal was shorter than normal (1.5 *vs.* 1.88 turns; 9.99mm *vs.* 15.98mm)(37). This raises the question whether more frequencies should be assigned to the basal array in CI programming, which depends upon whether apical peripheral processes can be stimulated. Where IP-II was present bilaterally, cochlea and SGN morphologies were symmetrical, illustrating that it may be possible to program bilateral implants similarly. Furthermore, abnormal SGN location may lead to unusual programming maps.

Two specimen had a history of meningitis. IEMs are a predisposing factor for recurrent bacterial meningitis, perhaps due to the poorly-developed modiolus permitting communication between cerebrospinal fluid and perilymphatic spaces(38). Visualisation of the cochlear lumen was obscured in these specimen due to post-meningitic changes, so comparison of intralabyrinthine compartments to normal cochleae was not feasible. However, inspection of the cribrose-internal acoustic meatus relationship did not demonstrate increased communication.

Endolymph compartments

Pathological enlargements of two endolymph-containing compartments, SM and EVA, were identified. The SM was either completely or partially expanded into the modiolus. Whilst the numbers in this study are low, EVA would seem to be associated with abnormal SM. This correlates mechanistically as both contain endolymph. As not all IP-II had abnormal SM/EVA, endolymphatic hydrops may not be an initial feature of IP-II but a marker of severity or secondary to the primary malformation. MicroCT of the IP-II mouse model suggested that pathogenesis was related to the loss of a hypoplastic bony septum due to endolymphatic abnormalities(32). It would be interesting to compare 3D morphology of SM in EVA, with and without IEM, to investigate whether this finding is isolated to IP-II.

Implications for choice of CI electrode

As with normal cochleae, selection of an electrode array should be patient-focused(39). Since CI mismatch to a patient's native place-frequency map may result in worse speech perception(40), an implant might be chosen to minimise tonotopic mismatch. Further work is required to establish the place-frequency map in IP-II, but the shorter Rosenthal's canal length may indicate that patients could benefit from a shorter array. Furthermore, a shorter array may limit trauma to abnormally-located peripheral processes and smaller ST cross-sectional area beyond one-full turn. Insertion beyond the latter may result in larger insertion forces, with associated trauma and inflammatory sequelae(41). To determine the impact of array length, future work should investigate the IP-II frequency map, as reported by Stakhovskaya(9).

The relative position of an array in the ST can also be chosen. Lateral wall implants are designed to minimise cochlear trauma, being situated along the outer wall of the ST. By contrast, perimodiolar implants are located medially, closer to the modiolus and SGNs. Whilst perimodiolar implants may lower SGN activation thresholds, they can cause more mechanical trauma(42). Two studies of normal cochleae demonstrated that patients with perimodiolar arrays had superior speech perception, although any advantage equalised by two-years post-insertion(39,43). Our current anatomical data are insufficient to support endorsement of one array over the other, and future work should model implant positions.

Limitations

One limitation is the small sample size, although it is the largest published histopathological series. Second is the lack of audiometry for every case. Finally, the historic nature of some specimens precluded in-depth analysis of patient symptomatology. Performing a post-mortem microCT or synchrotron imaging for future temporal bone cases with congenital malformations may assist in 3D

structural pathology, although this is limited by availability of cases and timing of procurement. The morphologic differentiation of IEM can be challenging on clinical imaging(44,45). Future studies should aim to combine post-mortem histology with clinical imaging. This may guide clinicians in differentiating IEM *in vivo*.

Conclusion

This study utilised 3D analysis to better understand the anatomy of IP-II malformations, and provides a basis for building a clearer understanding of the surgical and audiological implications for patients. Two types (A and B) of IP-II are suggested based on gross bony and SGN morphology. Findings suggest that IP-II represents a disease spectrum in terms of morphology and neural elements. The most extreme cases also had EVA and modiolar expansion of the SM, in association with classic IP-II findings. At the other end of the spectrum, the malformation was confined to the cochlea. CI surgeons should be mindful of the neural elements and short ST length when inserting an implant to avoid mechanical damage.

Acknowledgements

The authors would like to acknowledge Mary Fortune, statistician, for her statistical advice, and Iwan V. Roberts for his work in helping develop a custom MATLAB code. The authors also acknowledge the anatomical gifts of the temporal bone donors who enrolled in the NIDCD Temporal Bone Registry.

References

1. Boisvert I, Reis M, Au A, Cowan R, Dowell RC. Cochlear implantation outcomes in adults: A scoping review. *PLoS ONE*. 2020;15(5):e0232421. doi:10.1371/journal.pone.0232421

2. Jensen J. Malformations of the inner ear in deaf children. A tomographic and clinical study. *Acta Radiol Diagn (Stockh)*. Published online 1968:Suppl 286:3+.

3. Park AH, Kou B, Hotaling A, Azar-Kia B, Leonetti J, Papsin B. Clinical Course of Pediatric Congenital Inner Ear Malformations. *The Laryngoscope*. 2000;110(10):1715-1719. doi:10.1097/00005537-200010000-00029

4. Jackler RK, Luxford WM, House WF. Congenital malformations of the inner ear: A classification based on embryogenesis. *The Laryngoscope*. 1987;97(S40):2-14. doi:10.1002/lary.5540971301

5. Carlyon RP, Goehring T. Cochlear Implant Research and Development in the Twenty-first Century: A Critical Update. *JARO*. 2021;22(5):481-508. doi:10.1007/s10162-021-00811-5

6. Elfarnawany M, Alam SR, Rohani SA, Zhu N, Agrawal SK, Ladak HM. Micro-CT versus synchrotron radiation phase contrast imaging of human cochlea. *Journal of Microscopy*. 2017;265(3):349-357. doi:10.1111/jmi.12507

7. Li H, Helpard L, Ekeroot J, et al. Three-dimensional tonotopic mapping of the human cochlea based on synchrotron radiation phase-contrast imaging. *Sci Rep*. 2021;11(1):4437. doi:10.1038/s41598-021-83225-w

8. Glueckert R, Pfaller K, Kinnefors A, Rask-Andersen H, Schrott-Fischer A. The Human Spiral Ganglion: New Insights into Ultrastructure, Survival Rate and Implications for Cochlear Implants. *Audiol Neurotol*. 2005;10(5):258-273. doi:10.1159/000086000

9. Stakhovskaya O, Sridhar D, Bonham BH, Leake PA. Frequency Map for the Human Cochlear Spiral Ganglion: Implications for Cochlear Implants. *JARO*. 2007;8(2):220-233. doi:10.1007/s10162-007-0076-9

10. Sennaroğlu L, Saatci I. A New Classification for Cochleovestibular Malformations: *The Laryngoscope*. 2002;112(12):2230-2241. doi:10.1097/00005537-200212000-00019

11. Sennaroğlu L. Cochlear Implantation in Inner Ear Malformations — A Review Article. *Cochlear Implants International*. 2010;11(1):4-41. doi:10.1002/cii.416

12. Sennaroğlu L, Bajin MD. Incomplete partition type III: A rare and difficult cochlear implant surgical indication. *Auris Nasus Larynx*. 2018;45(1):26-32. doi:10.1016/j.anl.2017.02.006

13. Farhood Z, Nguyen SA, Miller SC, Holcomb MA, Meyer TA, Rizk HG. Cochlear Implantation in Inner Ear Malformations: Systematic Review of Speech Perception Outcomes and Intraoperative Findings. *Otolaryngol Head Neck Surg*. 2017;156(5):783-793. doi:10.1177/0194599817696502

14. Sennaroğlu L. Histopathology of inner ear malformations: Do we have enough evidence to explain pathophysiology? *Cochlear Implants International*. 2016;17(1):3-20. doi:10.1179/1754762815Y.0000000016

15. Dhanasingh A, Dietz A, Jolly C, Roland P. Human Inner-ear Malformation Types Captured in 3D. *Int Adv Otol*. 2019;15(1):77-82. doi:10.5152/iao.2019.6246

16. Sennaroğlu L. Histopathology of inner ear malformations: Do we have enough evidence to explain pathophysiology? *Cochlear Implants International*. 2016;17(1):3-20. doi:10.1179/1754762815Y.0000000016

17. Sennaroğlu L, Bajin MD. Classification and Current Management of Inner Ear Malformations. *Balkan Med J*. 2017;34(5):397-411. doi:10.4274/balkanmedj.2017.0367

18. Makary C, Shin J, Caruso P, Curtin H, Merchant S. A Histological Study of Scala Communis with Radiological Implications. *Audiol Neurotol*. 2010;15(6):383-393. doi:10.1159/000307345

19. Danielian A, Ishiyama G, Lopez IA, Ishiyama A. Predictors of Fibrotic and Bone Tissue Formation With 3-D Reconstructions of Post-Implantation Human Temporal Bones. *Otology & Neurotology*. 2021;42(7):e942-e948. doi:10.1097/MAO.0000000000003106

20. Geerardyn A, Zhu M, Wu P, et al. Three-dimensional quantification of fibrosis and ossification after cochlear implantation via virtual re-sectioning: Potential implications for residual hearing. *Hear Res*. 2023;428:108681. doi:10.1016/j.heares.2022.108681

21. Schindelin J, Arganda-Carreras I, Frise E, et al. Fiji: an open-source platform for biological-image analysis. *Nat Methods*. 2012;9(7):676-682. doi:10.1038/nmeth.2019

22. Gee AH, Zhao Y, Treece GM, Bance ML. Practicable assessment of cochlear size and shape from clinical CT images. *Sci Rep*. 2021;11(1):3448. doi:10.1038/s41598-021-83059-6

23. Cornwall HL, Marway PS, Bance M. A Micro-Computed Tomography Study of Round Window Anatomy and Implications for Atraumatic Cochlear Implant Insertion. *Otology & Neurotology*. 2021;42(2):327-334. doi:10.1097/MAO.0000000000002924

24. Valvassori GE, Clemis JD. The Large Vestibular Aqueduct Syndrome. *The Laryngoscope*. 1978;88(5):723-728. doi:10.1002/lary.1978.88.5.723

25. Nadol JB. Quantification of human spiral ganglion cells by serial section reconstruction and segmental density estimates. *American Journal of Otolaryngology*. 1988;9(2):47-51. doi:10.1016/S0196-0709(88)80007-3

26. Makary CA, Shin J, Kujawa SG, Liberman MC, Merchant SN. Age-Related Primary Cochlear Neuronal Degeneration in Human Temporal Bones. *JARO*. 2011;12(6):711-717. doi:10.1007/s10162-011-0283-2

27. Merchant S, Nadol JB. *Schuknecht's Pathology of the Ear*. 3rd ed. People's Medical Publishing House-USA; 2010.

28. Okayasu T, Quesnel AM, Reinshagen KL, Nadol JB. Otopathology in Kleefstra Syndrome: A Case Report. *The Laryngoscope*. 2020;130(8):2028-2033. doi:10.1002/lary.28380

29. Atturo F, Barbara M, Rask-Andersen H. Is the Human Round Window Really Round? An Anatomic Study With Surgical Implications. *Otology & Neurotology*. 2014;35(8):1354-1360. doi:10.1097/MAO.0000000000000332

30. Roland PS, Wright CG. Surgical Aspects of Cochlear Implantation: Mechanisms of Insertional Trauma. In: Møller AR, ed. *Advances in Oto-Rhino-Laryngology*. Vol 64. S. Karger AG; 2006:11-30. doi:10.1159/000094642

31. Koch RW, Ladak HM, Elfarnawany M, Agrawal SK. Measuring Cochlear Duct Length – a historical analysis of methods and results. *J Otolaryngol Head & Neck Surg*. 2017;46(1):19. doi:10.1186/s40463-017-0194-2

32. Ito T, Fujikawa T, Honda K, et al. Cochlear Pathomorphogenesis of Incomplete Partition Type II in Slc26a4-Null Mice. *JARO*. 2021;22(6):681-691. doi:10.1007/s10162-021-00812-4

33. O'Connell BP, Cakir A, Hunter JB, et al. Electrode Location and Angular Insertion Depth Are Predictors of Audiologic Outcomes in Cochlear Implantation. *Otology & Neurotology*. 2016;37(8):1016-1023. doi:10.1097/MAO.0000000000001125

34. Breitsprecher TM, Pscheidl A, Bächinger D, et al. Cochlear and Vestibular Volumes in Inner Ear Malformations. *Otol Neurotol*. 2022;43(8):e814-e819. doi:10.1097/MAO.0000000000003615

35. Dhanasingh A, Swords C, Bance M, Van Rompaey V, Van de Heyning P. Cochlear Size Assessment Predicts Scala Tympani Volume and Electrode Insertion Force- Implications in Robotic Assisted Cochlear Implant Surgery. *Front Surg*. 2021;8:723897. doi:10.3389/fsurg.2021.723897

36. Gifford RH, Dorman MF, Skarzynski H, et al. Cochlear Implantation With Hearing Preservation Yields Significant Benefit for Speech Recognition in Complex Listening Environments. *Ear & Hearing*. 2013;34(4):413-425. doi:10.1097/AUD.0b013e31827e8163

37. Kawano A, Seldon HL, Clark GM. Computer-Aided Three-Dimensional Reconstruction in Human Cochlear Maps: Measurement of the Lengths of Organ of Corti, Outer Wall, Inner Wall, and Rosenthal's Canal. *Ann Otol Rhinol Laryngol*. 1996;105(9):701-709. doi:10.1177/000348949610500906

38. Kepenekli-Kadayifci E, Karaaslan A, Atıcı S, et al. Recurrent Bacterial Meningitis in a Child with Mondini Dysplasia. *Case Reports in Pediatrics*. 2014;2014:1-3. doi:10.1155/2014/364657

39. Sturm JJ, Patel V, Dibelius G, Kuhlmey M, Kim AH. Comparative Performance of Lateral Wall and Perimodiolar Cochlear Implant Arrays. *Otology & Neurotology*. 2021;42(4):532-539. doi:10.1097/MAO.0000000000002997

40. Venail F, Mathiolon C, Menjot de Champfleur S, et al. Effects of Electrode Array Length on Frequency-Place Mismatch and Speech Perception with Cochlear Implants. *Audiol Neurotol*. 2015;20(2):102-111. doi:10.1159/000369333

41. Hrncirik F, Roberts IV, Swords C, et al. Impact of Scala Tympani Geometry on Insertion Forces during Implantation. *Biosensors*. 2022;12(11):999. doi:10.3390/bios12110999

42. Wanna GB, Noble JH, Carlson ML, et al. Impact of electrode design and surgical approach on scalar location and cochlear implant outcomes: Impact of Electrode Type and Approach on CI Outcome. *The Laryngoscope*. 2014;124(S6):S1-S7. doi:10.1002/lary.24728

43. Sharma RK, Smetak MR, Patro A, et al. Speech Recognition Performance Differences Between Precurved and Straight Electrode Arrays From a Single Manufacturer. *Otol Neurotol*. 2022;43(10):1149-1154. doi:10.1097/MAO.0000000000003703

464 44. Kontorinis G, Goetz F, Giourgas A, Lenarz T, Lanfermann H, Giesemann AM. Radiological
465 diagnosis of incomplete partition type I versus type II: significance for cochlear implantation.
466 *Eur Radiol*. 2012;22(3):525-532. doi:10.1007/s00330-011-2301-5

467 45. Reinshagen KL, Curtin HD, Quesnel AM, Juliano AF. Measurement for Detection of Incomplete
468 Partition Type II Anomalies on MR Imaging. *AJNR Am J Neuroradiol*. 2017;38(10):2003-2007.
469 doi:10.3174/ajnr.A5335

470

471

Legends

Figure 1. **A.** Example of normal cochlear histology (mid-modiolar section) **B.** Example of incomplete partition type-II (IP-II) cochlear histology (mid-modiolar section). **C.** Illustrative methodology depicting how to segment histology slides in Amira of IP-II cochleae. The separate components of the cochlea were segmented individually as follows: scala tympani, red; scala vestibuli, green; scala communis (fused scala tympani and vestibuli), yellow; scala media, blue; Rosenthal's canal, magenta **D.** 3D illustration of the position of the A-value and B-value.

Figure 2. Scala tympani findings. **A.** Estimating ST cross-sectional area from the round window to its fusion with SV, using a customised MATLAB script. **B-C.** Inferior view of the bony labyrinthine of IP-II cochleae, with two overall morphologies seen. Note the elongated middle turn and wide apical turn in **B** (3/R), as compared to the shorter middle turn and more narrow apical turn in **C** (7/L). **D-E** both also depict case 7/L. **D.** Scalae compartments: ST (red), SM (blue), SV (green), SC (yellow). **E.** ST compartment alone. **F.** Mean 3D cross-sectional area (and standard deviation in paler shading) of scala tympani of IP-II cochleae, as compared to normative data (n=66, unpublished data derived from microcomputed tomography imaging).

Figure 3. 3D SM morphology. **A-C.** Exemplar histopathological slides of three different IP-II cases. Particular reference is made to the appearance of the scala media (SM – asterisk *). In C, the SM is completely expanded into the modiolus (A: 7/L; B: 1/L; C: 6/L). **D-F.** The corresponding SM 3D reconstructions are below each histopathological image. Note the spectrum of appearance of SM from normal (D) to additional SM compartment (E) to complete expansion into the modiolus (F), yet SM is separate in all cochleae.

Figure 4. Spiral ganglion counts **A.** 3D plot of spiral ganglion (SGN) location (purple) in comparison to the cochlea (transparent grey) with apical SGNs of case 1/L. Note the relatively sparse numbers of SGNs projecting apically. The appearances do not feature the classic 'twisted' view seen with normal apical projections, as per Wu *et al.* 2023(under peer review). **B-C.** Spiral ganglion cells failed to migrate towards the superior modiolus, relative to degree of rotation, with 0^{o} at the round window, case 7/L. **D-E**. The same cochlea as Figure 3B,C **D.** Population of SGNs at the modiolar base that failed to migrate superiorly (blue magnifying box). **E**. Stacked unstained histology sections illustrating that the peripheral axons (highlighted in red) of this extra clump of SGNs (highlighted in blue) traverse superiorly through the scalae to innervate the apical most organ of Corti. They are vulnerably located within the scalae without a bony covering. **F**. Spiral ganglion cells located in the internal auditory meatus (black magnifying box, case 5/L)

Figure 5. 3D plots depicting SGN location (purple) versus scala media location (blue), sub-divided into type A and type B IP-II cochleae. The total SGN count (and age-matched control percentage) and proportion of SGN located in basal modiolus are presented. Accurate SGN counts were not possible in cochlea 4R/L

Table 1. 3D quantitative assessments of IP-II cochleae. SD, standard deviation; ST, scala tympani. *Case 2 showed 1.5 turns of isolated scala tympani before fusing with scala vestibuli, then split again into an isolated ST compartment for a further 0.25 turn almost immediately. ^Normal SGN count data obtained from published values of age-matched controls(27). *This row is comprised of average published values for normal cochlea, to enable ease of comparison. This data was not obtained during this study.

Supplementary Materials Legends

Supplementary Material 1. Search Terms for National Institute on Deafness and Other Communication Disorders (NIDCD) National Temporal Bone Hearing and Balance Pathology Resource Registry (NIDCD Registry)

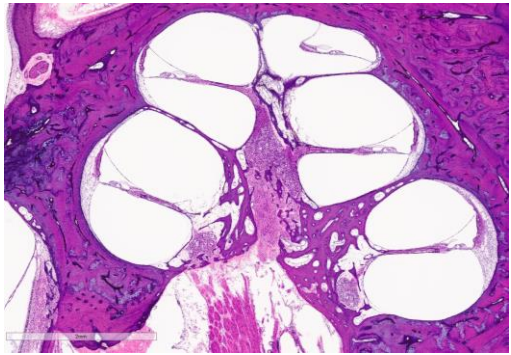
Supplementary Material 2. A. Measurement of vestibular aqueduct midpoint width. **B.** Measurement of vestibular aqueduct opercular width, defined perpendicular to the segment of the petrous ridge across from the tip of the opposite bony ridge. **C.** Example of SGN identified by the machine learning algorithm.

Supplementary Material 3. Summary of all cases identified from database searching

Supplementary Material 4. **Descriptors of IP-II cochleae**. ^Shape of otic capsule, described as type A (elongated middle turn, with a apical turn of similar width to the middle) or type B (shorter middle turn, with an apical turn of smaller width). *vestibular morphology was qualitatively assessed by an experienced histopathologist. MI, myocardial infarction; NS, not specified; CAD, coronary artery disease; SNHL, sensorineural hearing loss; IAC, internal auditory canal; EVA, enlarged vestibular aqueduct; VA MP, vestibular aqueduct midpoint width (mm); VA op, vestibular aqueduct operculum width (mm); SC, scala communis; IS, interscalar ridge; OoC, organ of corti; SM, scala media; BT, basal turn; NV, not visible due to post-meningitic changes; PSCC, posterior semicircular canal; MT, middle turn

Supplementary Material 5. RW and niche findings of a left cochlea. Normal surgical positioning of the head (pinna would usually be retracted anteriorly) to demonstrate surgical orientation of the cochlea. **A.** 3D reconstruction of promontory/niche (beige), round window membrane (green) and stapes footplate (light blue) orientated in the surgical plane (1/L) **B-C**. Various positions of the round window membrane: **B.** More inferiorly oriented RW **C.** More posteriorly oriented RW. Round window membrane (green), crista fenestra (dark blue), secondary spiral lamina (magenta), basilar membrane (yellow), osseous spiral lamina (red). Notably in 4D, the ST and SV fuse to become SC, but then temporarily separate before re-joining at the apex.

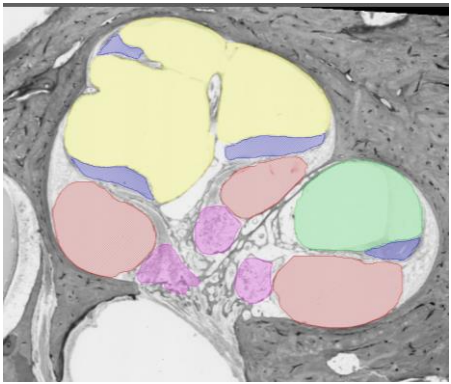
A



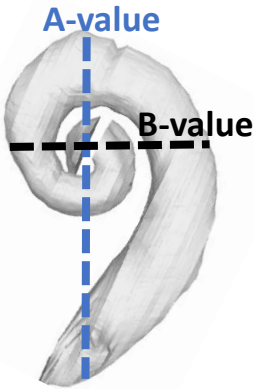
B

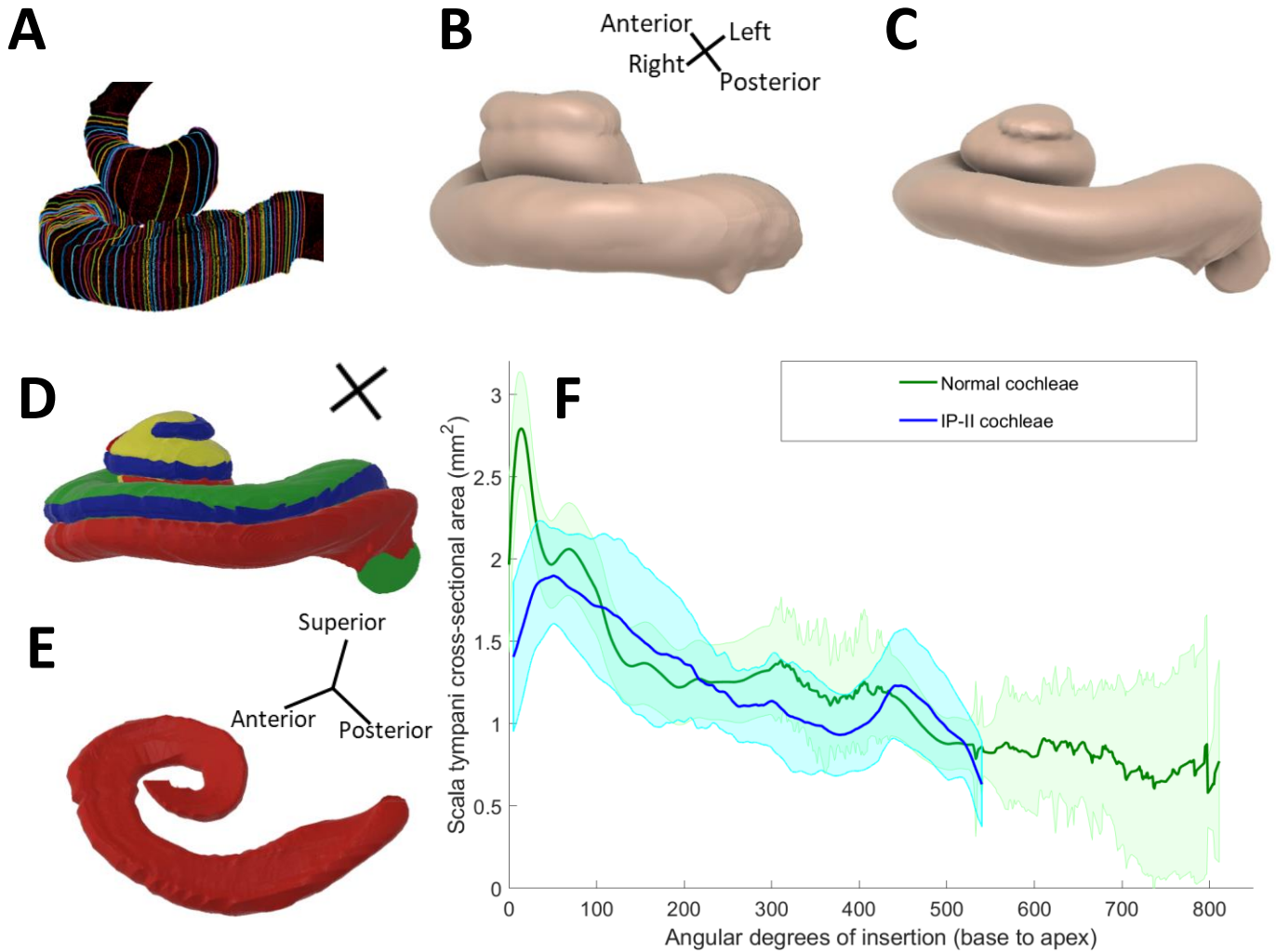


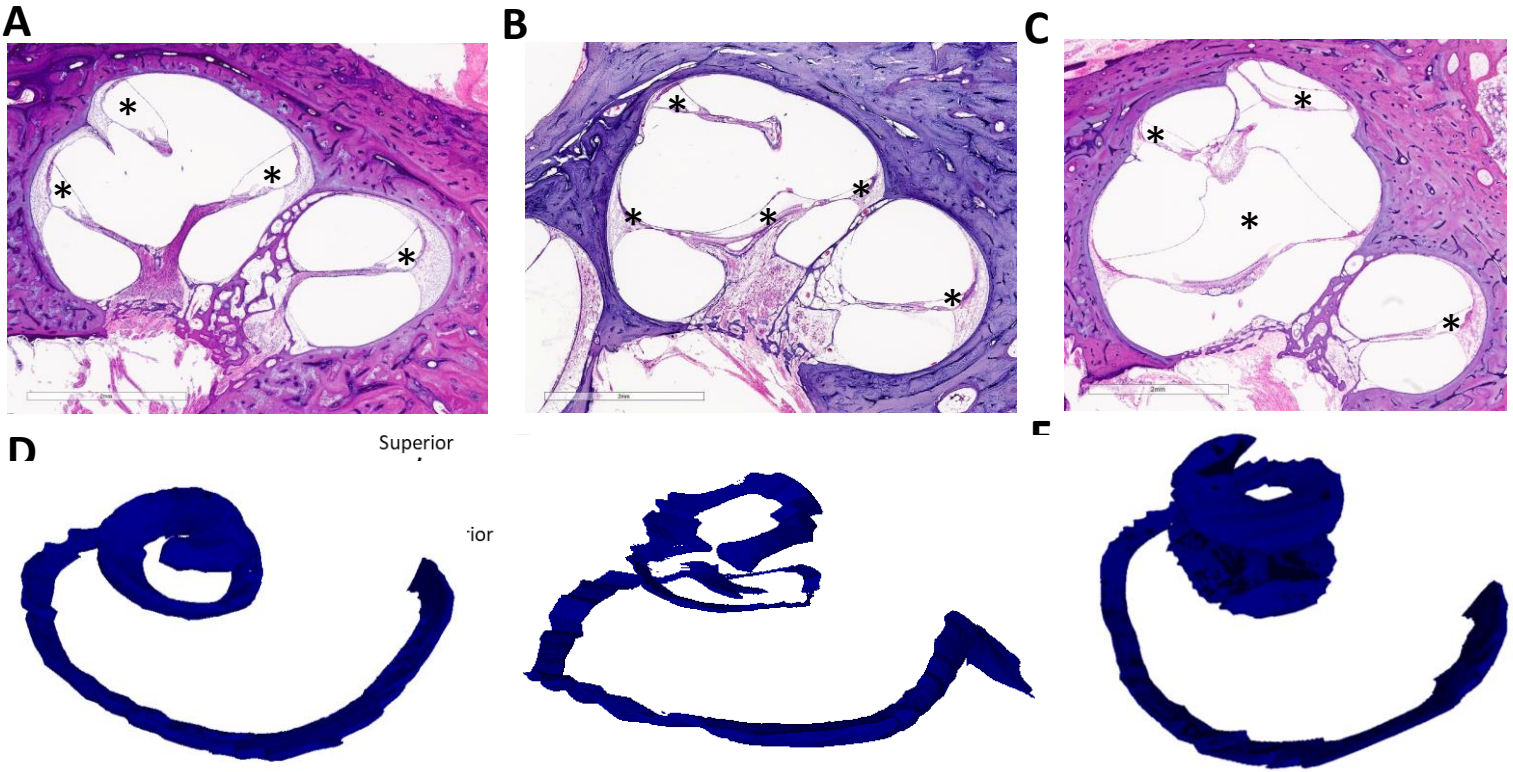
C

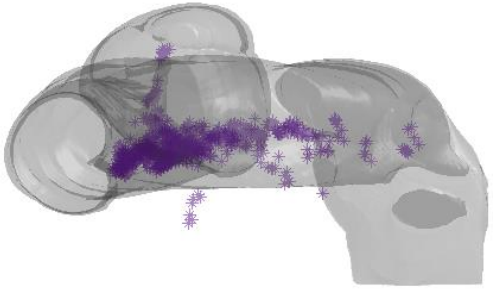


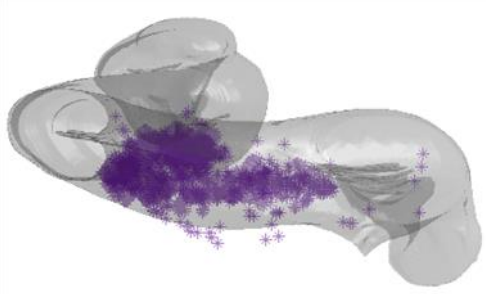
D

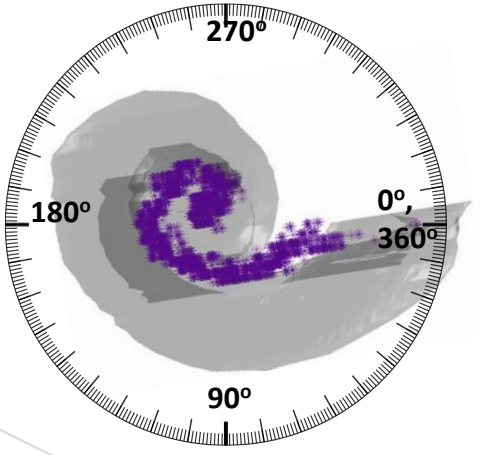


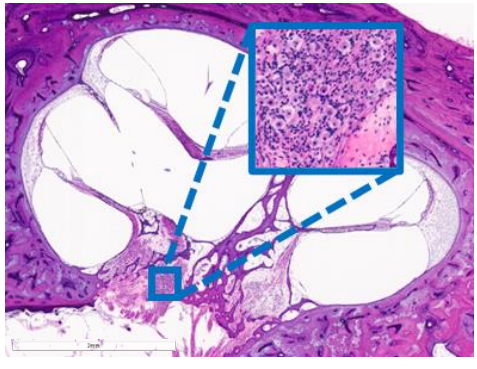

A
B
Anterior
Left
Right
Posterior
C
D
E
Superior
Anterior
Posterior
F
Normal cochleae
IP-II cochleae
Scala tympani cross-sectional area (mm2)
Angular degrees of insertion (base to apex)
0
0.5
1
1.5
2
2.5
3
0
100
200
300
400
500
600
700
800

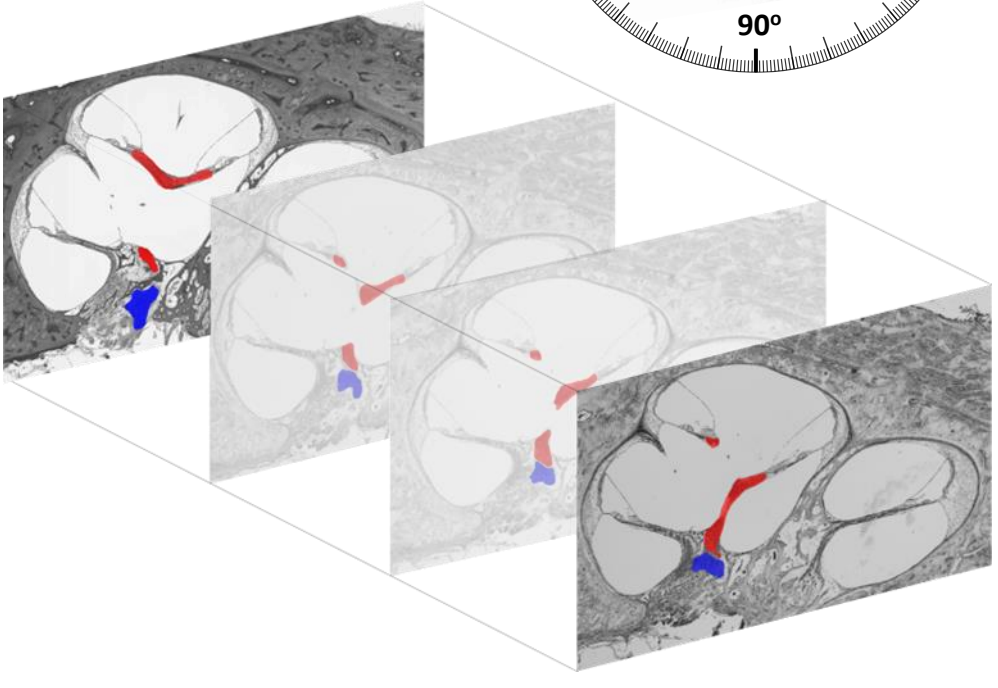

A
B
C
D
Superior
E

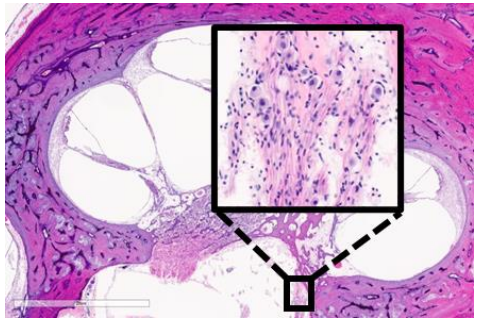




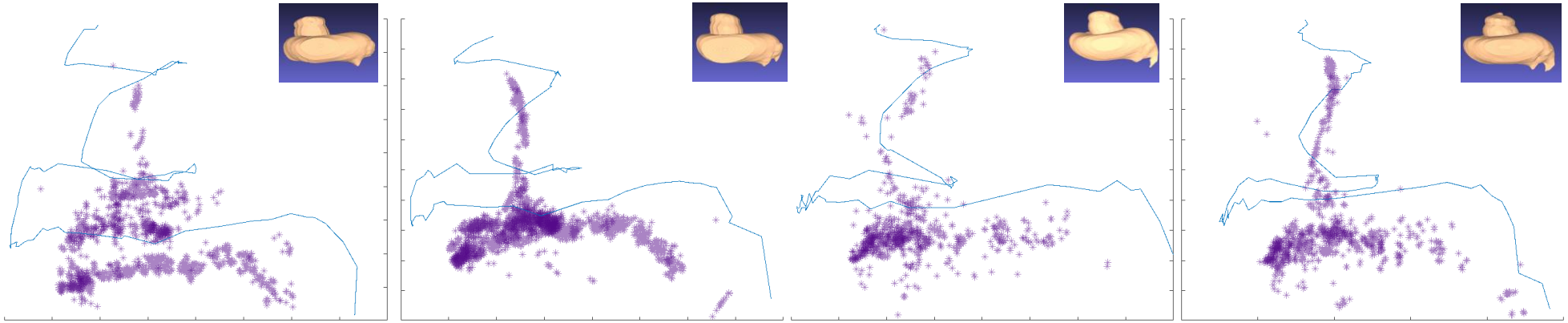

270°
180°
0°,
360°
90°





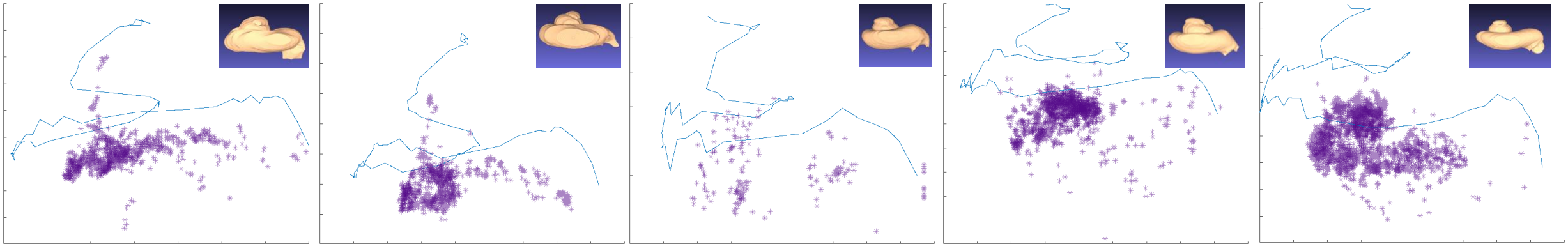


IP-II Type A: Average age-adjusted SGN 50% (range 32-80%)



Cochlea identifier	3/R	3/L	6/R	6/L
Absolute total SGN count (%)	10,037 (49%)	16,368 (80%)	5,576 (32%)	6,943 (40%)
Proportion in basal modiolus (%)	77%	76%	85%	78%

IP-II Type B: Average age-adjusted SGN 45% (range 5-90%)



Cochlea identifier	1/L	1/R	2/L	5/L	7/L
Absolute total SGN count (%)	8,004 (40%)	7,208 (36%)	1,292 (5%)	12,396 (54%)	20,692 (90%)
Proportion in basal modiolus (%)	98%	98%	100%	100%	100%